



HAL
open science

Experimental analysis of Lagrangian paths of drops generated by liquid/liquid sprays

Gagan Kewalramani, Bowen Ji, Yvan Dossmann, Michel Gradeck, Nicolas
Rimbert

► **To cite this version:**

Gagan Kewalramani, Bowen Ji, Yvan Dossmann, Michel Gradeck, Nicolas Rimbert. Experimental analysis of Lagrangian paths of drops generated by liquid/liquid sprays. *Experiments in Fluids*, 2022, 63 (9), pp.147. 10.1007/s00348-022-03496-5 . hal-03765626

HAL Id: hal-03765626

<https://hal.univ-lorraine.fr/hal-03765626>

Submitted on 31 Aug 2022

HAL is a multi-disciplinary open access archive for the deposit and dissemination of scientific research documents, whether they are published or not. The documents may come from teaching and research institutions in France or abroad, or from public or private research centers.

L'archive ouverte pluridisciplinaire **HAL**, est destinée au dépôt et à la diffusion de documents scientifiques de niveau recherche, publiés ou non, émanant des établissements d'enseignement et de recherche français ou étrangers, des laboratoires publics ou privés.

Experimental analysis of Lagrangian paths of drops generated by liquid/liquid sprays

Gagan Kewalramani^{1*†}, Bowen Ji^{1†}, Yvan Dossmann^{1†}, Michel Gradeck^{1†} and Nicolas Rimbert^{1†}

^{1*}LEMETA CNRS, Université de Lorraine, 2 Avenue de la Forêt de Haye, Vandoeuvre-lès-Nancy, 54518, Lorraine, France.

*Corresponding author(s). E-mail(s):

gagan-vikram.kewalramani@univ-lorraine.fr;

Contributing authors: bowen.ji@univ-lorraine.fr;

yvan.dossmann@univ-lorraine.fr; michel.gradeck@univ-lorraine.fr;

nicolas.rimbert@univ-lorraine.fr;

[†]These authors contributed equally to this work.

Abstract

In the present study, Lagrangian measurements of drop motion of a two-phase spray are analyzed to estimate the collision, fragmentation, size, and velocity field of the drops. An experimental setup is designed to record fluorescence images of drops, illuminated by a planar laser sheet. The recorded images are then processed with a commercially available Lagrangian tracking software, *Track*. The methodology for particle identification, tracking, and size approximation in *Track* in the near interface region of spray is stated. With the stated methodology, the information about size, velocity, fragmentation, collision, and change in the shape of the drops are obtained. The effectiveness of the developed methodology is tested against synthetically produced images and is then applied to a liquid/liquid jet. Similar behaviors for dispersed phase fragmentation-collision and mass fragmented along axial location normalized by breakup length of the jet are reported.

Keywords: Sprays, Lagrangian, fragmentation, collision

1 Introduction and related literature

Two-phase flows with drops of various sizes occur in various industrial (eg. sprays, nuclear safety) and environmental applications (eg. clouds). Analysis of the dynamics of dispersed flows often requires studying phenomena like coalescence, fragmentation, and changes in the shape of drops. Understanding this phenomenon is important in various situations, for example, coalescence of inertial drops in clouds determines rain formation and size distribution of the drops in sprays affects combustion. This work presents a non-intrusive (using index matching) estimation of fragmentation, collision, size and velocity of the drops in liquid/liquid jets with Weber number in the range [279 – 5256] and Reynolds number in the range [295 – 1813] using planar images. Various non-intrusive measurement methods in sprays such as, particle image velocimetry (PIV)[1], Planar laser-induced fluorescence (Planar LIF), Phase doppler anemometry (PDA), Shadowgraphy, and Mie Scattering imaging have been already used in literature.

Shadowgraphy is one of the simplest techniques for planar visualization of the dispersed phase in dilute regions. The drop size in a shadowgraph image is a result of the convolution of point spread function from illumination and drop diameter, therefore contrast of the drop in the images can be used to obtain its size in the depth of field, as demonstrated by Blaisot *et.al* [2]-[3]. Nishino *et. al* [4] have also demonstrated that with suitable calibration on the Stereo-shadowgraph, diameter of 10–500 μm with the accuracy of $\pm 4 \mu\text{m}$ can be estimated. Recently, Asgarian *et. al* [5] have presented a methodology to remove the out-of-focus particle on shadowgraph images using the gradient of the drop image. Even with the recent developments, analysis of drops for a spray with the shadowgraph technique is difficult due to high concentration of drops. However, with the use of laser sheets, illumination only in the desired plane of spray can be obtained, therefore planar laser sheet is used in present experiments. Using laser illumination at a plane, drop diameter can be predicted by calibrating its contrast and intensity in the depth of field as demonstrated by Kashdan *et.al* [6]. Akhmetbekov *et. al* [7] have developed Planar-fluorescence bubble imaging technique to predicted the size and velocity of the bubble using empirically correlation of the reflection of the laser at the interface.

The technique that obtains visualization using a fluorescing dye to radiate fluorescence when illuminated by a laser sheet is known as the Planar LIF technique. In planar LIF, only the drops present in the laser sheet are illuminated and thus can be analyzed. With the prior knowledge of absorption illumination characteristics of dye, the intensity of the drop measured by the detector can be directly related to the volume fraction (cf. Crimaldi [8]) and temperature (cf. Dunand *et.al* [9]) measurement. However, for sprays Deskmukh and Ravikrishna [10] and Desentes *et.al* [11] have presented methods to account for attenuation effects due to absorption, non-homogenization, and Mie scattering of the laser sheet for volume fraction measurement. Kannaiyan *et.al* [12],

Koegl *et. al* [13] and Zimmer *et. al* [14] have demonstrated accurate measurement of the Sauter mean diameter (SMD) by separating detection of LIF and Mie scattering signals with optical filters. Kristensson *et. al* [15] have developed methods to remove the blurring effect with multiple scattering from the laser sheet illumination referred as SLIPI (structured laser-induced planar illumination). Abu-Gharbieh *et. al* [16] have also developed an iterative approach to correct attenuation due to scattering with reasonable accuracy. Considering the effectiveness of the fluorescence for sprays from previous studies, a fluorescing dye is used in present experiments to identify and analyze the drops in laser sheet.

The Lagrangian tracking method can be used with the shadowgraphy or planar LIF to measure the velocity of droplets [17], usually referred to as Droplet Tracking Velocimetry (DTV). The fundamental concept of obtaining velocity from DTV is similar to Particle Tracking Velocimetry (PTV). The simplest tracking methods used in DTV searches for the nearest particle in the next frame. Cierpka *et. al* [18] have developed a higher-order multi-frame particle tracking method, which uses a predictive method based on previous frames positions to improve the performance of tracking. Wu *et. al* [19] have used Kalman filtering for the prediction of particle positions, which reduces the positioning error in particle tracking. Here in the present analysis, we have also used Kalman filtering for Lagrangian tracking of identified particles. The tracking information can also be used to analyze collision. Recently, Kearney and Bewley [20] presented a three-dimensional Lagrangian tracking of the drops. After anticipating the trajectories of drops, the collision can be determined. Bordas *et. al* [21] also used the similar methodology of identifying collision along the anticipated particle trajectories if drop boundaries merge. To find the exact shape of the particle, Kearney and Bewley [20] have used Pratt Walking fitting algorithm to fit the shape of the drop with the set of circles to determine the drop edge. Here we present a collision estimation based on two dimensional images.

With different methods and procedures cited in the literature for obtaining volume fraction; detecting drops and their size and later tracking, we present an methodology based on pixel intensity information using the commercially available software *Track* [22] in the dense region in sprays. Drops of various sizes are produced in sprays, for example it is narrow for injector in paints and very wide for the injector in turbines. Dechelette [23] has summarized various size distribution present in sprays. In literature, several different fragmentation mechanisms exist in sprays and are described by Gorokhovski and Herrmann [24] and Villermaux [25]. In the present paper we describe and test a methodology to identify fragmentation and collision for sprays.

This paper is organized as follows. First, the details of the experimental setup developed is presented in section 2. The parameters that are used in the software are detailed in section 3. The results obtained from *Track* are later post-processed to obtain relevant information, the post processing procedure being also explained in section 3. The verification of the collision-fragmentation

methodology and volume fraction and velocity is evaluated in section 4. The identified fragmentation and collision mechanisms for sprays generated from experiments are also discussed in section 4. Later, the results of number of collision/fragmentation events and fraction mass fragmented axially are analyzed briefly in section 4. At last, the conclusion are drawn in section 5.

2 Experimental campaign

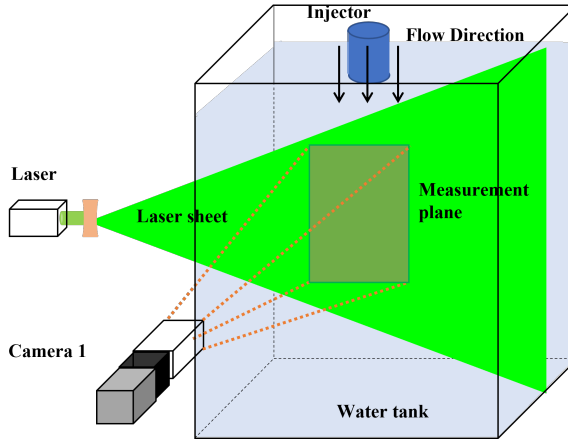


Fig. 1 Schematic of experimental setup with its component.

The schematics of the experimental arrangement used for injection of Cargille fluid into water tank is presented in figure 1. A pneumatic controlled injector attached to the nozzle is submerged at the top of the water tank (dimension of tank $50 \times 50 \times 40 \text{ cm}^3$). Different velocities of the jet in the injector are imposed by varying pressure through a manual pressure valve. A transparent fluid (produced by Cargille-Sacher laboratory) with an optical index equal to water (refractive index 1.3330) but heavier and more viscous than water, referred to as Cargille fluid is injected in a water tank. The physical properties of the Cargille fluid and water are denoted with the subscript L and C respectively such as, $\rho_L = 1896.52 \text{ kg/m}^3$, $\mu_L = 26.02 \text{ mPa}\cdot\text{s}$, $\rho_C = 998.2 \text{ kg/m}^3$ and $\mu_C = 1.05 \text{ mPa}\cdot\text{s}$. The surface tension between the fluids is $\sigma = 0.0265 \text{ N/m}$. The design details of the injector used can be found in Hadj-Achour *et.al* [26].

A laser sheet with wavelength 532 nm is generated by the laser source manufactured by Laser Quantum (type finesse), which is used to illuminate the central plane of the jet. The laser from the laser sources is expanded using a diverging lens (laser sheet through a concave lens). **Concave lens of focal length around 15 mm is used to generate with divergence angle 9.4°** . The thickness of the laser sheet obtained is such that the waist width of the laser sheet is $2.25 \pm 0.25 \text{ mm}$. In order to identify Cargille fluid in laser sheet, it is mixed with

Pyromethene 597-(8C9) dye of molar absorption coefficient (at 524 nm) $5.25 \cdot 10^4$ L/(mol. cm). A dye concentration of 10^{-6} grams per unit gram of liquid is used in all our experiments. During the course of the experiments, the high-speed CMOS sensor camera of the Phantom v710 camera records images with a frame rate of 9000 frames per second. It should be noted that a high frame rate is selected in order to accurately track detected particles. An optical lens of 150 mm focus length (aperture F2.8) records images close to the injector. Images with 1280 pixels along flow direction and 640 pixels along width are recorded such that one pixel corresponds to $99.5 \mu\text{m}$. Images from various jets with different nozzle diameters (D2, D3, and D4) and at different injection velocities (U_0), are recorded as stated in table 1. The nozzle diameters of 2 mm, 3 mm and 4 mm are used for experiments with names D2, D3 and D4 respectively. The images from the experimental setup are analyzed after the steady state is reached *i.e.* the images of transient part are excluded. For each of the cases stated in table 1, 1500 images at the steady state are analyzed in the result section 4.

Table 1 Velocity (in m/sec), Diameter, Reynolds number (Re) and Weber number (We) for various jets.

Exp:	U_0	Re	We	Exp:	U_0	Re	We	Exp:	U_0	Re	We
D2V1	1.92	295	279	D2V2	2.96	455	663	D2V3	5.46	838	2248
D3V1	1.62	375	300	D3V2	3.13	764	1245	D3V3	5.96	1375	4027
D4V1	1.72	530	449	D4V2	3.05	938	1408	D4V3	5.90	1813	5256

The definition of Reynolds number, Weber number and Ohnesorge number are recalled in equation 1. For the conducted experiments, density ratio ($\frac{\rho_L}{\rho_C} = 1.9$) and viscosity ratio ($\frac{\mu_L}{\mu_C} = 24.78$) are constant. Since the same fluid is used for each experiment, the Ohnesorge number only varies slightly with different diameter of nozzle.

$$We = \frac{\rho_C U_0^2 D}{\sigma} \quad Re = \frac{U_0 D}{\nu_L} \quad Oh = \frac{\mu_L}{\sqrt{\rho_L \sigma D}} \quad (1)$$

For the lens F2.8 with focal length 150 mm, the maximum chromatic aberration is less than 0.03 % of frame height and geometric distortion as -0.004 %. Since distortion correction for images are minimal, a simple constant magnification calibration of images is used in present experiments.

3 Methodology

In the present study, flow visualization in planar LIF is obtained by using two immiscible fluids (Cargille fluid and water) with matched refractive index such that no light is deviated. Intensity information from the camera can be used to

identify drops, track them and obtain their size. The processing methodology of images is presented in this section.

3.1 Droplet tracking with *Track*

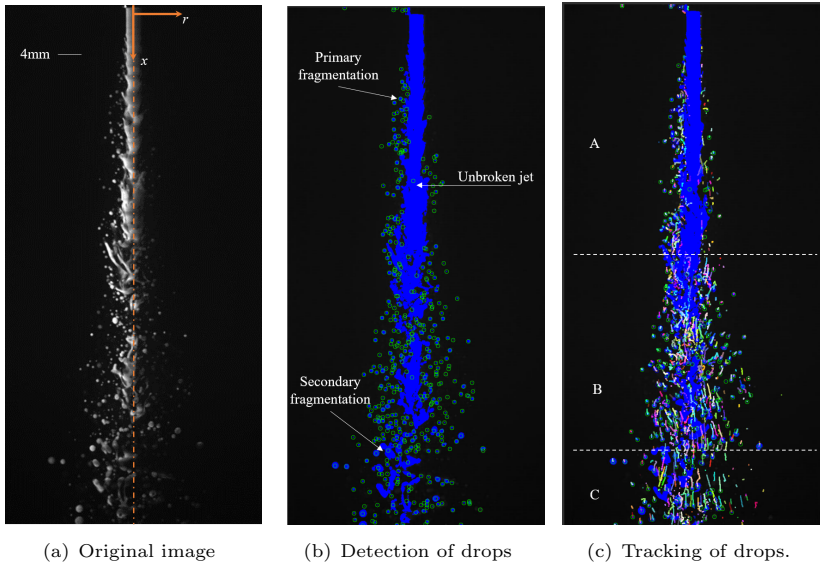


Fig. 2 Detection methodology in *Track*.: The sample image obtained from camera, the identified drop using fluorescence and, tracking of drop after few frames are shown in figure 2(a), 2(b) and 2(c) respectively

Experimental images obtained are processed in *Track*, a Lagrangian particle tracking software developed by APREX Solutions [22]. The general principle of working of *Track* is the same as any other PTV method, except that particles can be of any size and shape. As an initial step, images are initially "cleaned" from noise or unwanted object by background subtraction. There are various spatial filtering option provided in *Track* that can used to modify the image intensity in the images to assist the detection of particle, but in the present experiments none were used to preserve the intensity information of the drops. The second step that differentiates *Track* from standard PTV is setting the detection criteria for selection of drops. The details of intensity based detection and tracking of the *Track* is similar to TRACE algorithm detailed in Brochard *et.al* [27]. Droplets in the images are identified with a pixel clouds detection method, *i.e.* continuous region of pixels with intensity value larger than the threshold intensity value. The total number of pixels for each identified drop is calculated to obtain the area of the drop identified. Criteria based on size, aspect ratio, intensity value with multiscale spatial threshold (refer Brochard *et.al* [28] for example) are available for detection in *Track*. In the present

study we have only used detection criteria based on intensity threshold *i.e.* a minimum value of fluorescence intensity threshold for detection of drop.

Since only a part of the spray is illuminated by the laser sheet with Gaussian profile in the transverse direction, partially illuminated drops (at the edge of laser sheet) with very low fluorescence intensity are always present in the field of view. In the dense regions in sprays, a low value of threshold intensity selection results in the detection of partially submerged particles (with low-intensity) as part of drops present at the center laser sheet and overestimates area of drops. Whereas, a very higher value of threshold intensity selection causes the missing of smaller particles. The threshold value selection is dependent of laser power, camera used, dye concentration characteristic and should be selected carefully such that the boundaries of targeted drops (at the center of laser sheet) are identified. With a 8 bit images available in *Track* (with intensity value range 0 to 255), an intensity threshold value of 45 was used. Selection of threshold value for particle is also affected by attenuation and vertical divergence of laser sheet. Detection of particle with small sizes are more significantly affected by the these effect as compared to larger particles. This is because larger particle near the center of the laser sheet emit all the fluorescence in the laser sheet and thus give large intensity. Therefore in the analysis, minimum area A_{min} is used (determined later in section 4.1). The results of particle of size area smaller than A_{min} are excluded from estimation of fragmentation and collision as they are more sensitive to threshold selection.

The identified drops are finally tracked. In *Track*, three options to track objects are provided. (i) the minimization of the total mean square displacement (also used in Brochard *et.al* [28]), (ii) A predictive tracking based on Bayesian theory (refer Von der Linden *et.al* [29] for details) (iii) and a combination of both techniques. In the present experiments, Kalman filtering (for details refer Yagoh *et.al* [30]) as a predictive tracking method is used. The predictive tracking option based on Bayesian theory permits to configure a Kalman filter [29], to set a range of acceptable accuracy for the prediction. For tracking drop, the position of a drop in the $n + 2$ frame is predicted based on its previous positions (n ; $n + 1$ frame) with a certain tolerance. This makes it possible to predict the trajectory of objects by smoothing the data on their position, speed and acceleration at each instant, eliminating the disturbance due to noise or measurement errors, and to correctly recover positions of objects hidden by occlusion. For the images used in the present analysis a tolerance of 10 pixels with Kalman predictive measurement is used. This tolerance is selected based on maximum pixel displacement for the largest jet velocity. A shorter tolerance results in an increase in number of trajectories which would have shorter life time and vice versa. Since two methods (detailed in section 3.2) based on continuation and non-continuation of trajectories are used, the effect of tolerance of fragmentation/collision estimation is not significant. Recently, Metivier *et.al* [31] and Ou *et.al* [32] have also used *Track*.

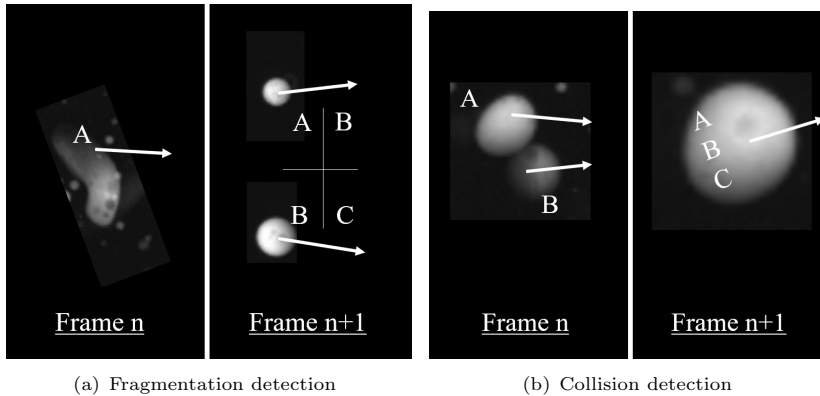


Fig. 3 Schematic describing fragmentation and Collision detection methodology

The images analyzed with the **described** procedure for the experiment D4V1 are shown in figure 2. The original image, the image after detection and trajectories of the detected particles are shown in figure 2(a), 2(b) and 2(c) respectively. Due to laser attenuation near the nozzle area particles on the right side are not illuminated sufficiently. However, after the breakup length, it can be observed that the attenuation effects are **weak enough** to allow particle detection. The unbroken part of the jet near the nozzle, referred as potential core hereafter is **also** considered as a drop. The significance of this detection is discussed in section 4.

Width and height are determined by fitting a bounding box around the detected objects. The information about trajectories (velocity, acceleration), area (A), width (W), height (H) and intensities (mean (I_{mean}), max (I_{max})) for an unique identified drop, **also refereed as ID** are obtained with *Track*. For the images with low concentration and low velocity, each ID corresponds to a drop. Since near the interface, we have regular fragmentation and collision and also the motion of drop within the thickness of the laser sheet, the area of the drop needs to be processed to estimate its size. Although the selection of the minimum threshold value of particle detection removes **out-of-focus** particles in the depth of the laser sheet, there is still significant change in the **drop area** due to the transverse movement in the depth of the field. Therefore geometrical and intensity data for each ID are **discriminated to identify drop**, as discussed in next section.

3.2 In plane fragmentation/collision and size estimation

To accurately estimate the collision/fragmentation processes, it is necessary to have information of the location of the particle in 3 directions at all times. Since we are processing only two-dimensional images, the procedure used for estimation in-plane fragmentation and collision is stated **only**. Drops that remain in the laser sheet before and after the collision/fragmentation events can be analyzed with the stated procedure. The schematic of an in-plane fragmentation

and collision events is shown in figure 3(a) and 3(b) respectively. Consider a drop with ID A fragmenting at time frame n resulting in the formation of two drops. If the trajectory of a daughter is close to the trajectories predicted by the Kalman method, then A fragments into $A\&B$ else it fragments into $B\&C$. Similar results are observed for the two colliding drops. For two colliding drops $A\&B$, the resultant drop can be either A or B if the position predicted by the Kalman method ID is close to ID A or B respectively or else it is identified as ID C . Since there are two possibilities of identifying fragmenting and collision events (with and without continuation of ID), we use two methods to identify the events. Method I is used to identify events based on the continuation of the ID and method II is used to identify events based on the occurrence of new ID.

For identifying the events with method I, we track 3 parameters along the trajectories viz Area (A), normalized change in area ($\frac{dA}{A}$), the change in magnitude of velocity ($\frac{dV_{\text{mag}}}{V_{\text{mag}}}$) where $V_{\text{mag}} = (v_x^2 + v_y^2)^{1/2}$. The information of particle shape using width (W), height (H) and area is also used. The constraint used with method I are as follows:

(i) One of the primary features of capturing fragmentation/collision with the continuation of ID is the change in area. A change in the area can also occur due to the motion of the drop in the direction of laser sheet thickness or due to drop overlap. However, change in area due to overlap is not sustained for a long time and occurs only for a few frames, and also changes in area due to traverse motion are gradual. Therefore a sudden change in the area that is also sustained along the trajectories is considered as a candidate for fragmentation/collision. To confirm collision and fragmentation additional constraints in (ii), (iii) and (iv) are checked.

(ii) The magnitude of change in area with respect to area ($\frac{dA}{A}$) with time is also observed. In order to ensure conformity, the constraints of the maximum deformation of drop as approximated by Hsiang and Faeth [33] and Rimbart *et. al* [34] as, $(\frac{dA}{A})_{\text{max}} = \frac{1}{(1+0.019We)^3}$ is used. With $We < 10$ for non fragmenting drops, sudden deformation with $\frac{dA}{A} > 0.2$ is considered as candidature for fragmenting or colliding drops.

(iii) At the locations satisfying both the above-stated conditions, the information of the shape of the drops is also analyzed. During collision/fragmentation event, the shape of the drop is corrugated and thus is different from an ellipse. Therefore the equivalent area of ellipse is calculated (A_{pre}) based on the width (W) and height (H) of an ID. The location with significant difference between the A_{pre} and known area (A) is considered.

(iv) Additionally, the momentum of drops changes abruptly during a collision/fragmentation event. With the Stokes equation for momentum of particle, the change in momentum can be stated as, $\frac{dV_{\text{mag}}}{V_{\text{mag}}} = -\frac{d\tau}{St} \left(1 - \frac{u_f}{V_{\text{mag}}}\right) + \mathbf{S} \frac{d\tau}{V_{\text{mag}}}$. In the stated equation, St is Stokes number ($\frac{\rho_L d_p}{9\rho_c \mu_c t_\eta}$), $d\tau$ is non-dimensional time ($\frac{t}{t_\eta}$), t_η is Kolmogorov time and \mathbf{S} is additional term representing the

abrupt change due to collision. Based on our observation for colliding drops events, $\frac{dV_{\text{mag}}}{V_{\text{mag}}} > 0.2$ are considered as collision or fragmentation.

Drops satisfying all stated conditions at a given time are considered to be either collided or fragmented based on increase or decrease in area respectively. For estimating the fragmentation and collision events with method II, we note the birth and death location of each identified ID. The IDs with the birth frame next to the death and at a location very close to each other are again tested with the constraint (ii) and (iii).

The stated method is only limited to identify the events when both the colliding or fragmenting drops have approximately equal sizes. For the procedure used to identify collision or fragmentation of particle, the normalized change in the area $\left(\frac{dA}{A}\right)$ of particles along its trajectory is observed. For a drop fragmenting in two drops (with diameter d_1 and d_2) or two drops (with diameter d_1 and d_2) colliding into bigger drop, their diameter ratio $\frac{\min[d_1, d_2]}{\max[d_1, d_2]}$ is related to the normalized change in area. A very small change in normalized area is obtain if the diameter ratio is large or small. Since small change in normalized area of particle can also occur due to transverse motion of the particle, it becomes difficult to distinguish between small normalized area change due to transverse motion or due to collision/fragmentation of particle with very large or small diameter ratio. For the drop with the smaller area, there is a large change in relative area. In order to check the accuracy and the limit of its applicability in terms of A_{min} and diameter ratio, the method is evaluated against synthetic images in the next section. Using the information of intensity of the ID during its trajectory, we assume that the maximum intensity of the drop exists when the particle is exactly at the center of the laser sheet. With this assumption, the area of particle where its intensity is maximum is considered as the area of the particle.

4 Validation and Results

In the present section, the methodology stated in previous section is validated. Later an interpretation of results obtained is stated.

4.1 Validation of collision-fragmentation method

In this subsection, the methodology stated in section 3.2 is tested against synthetically generated images. To validate the procedure, various test cases with 1500 images are developed with parameters stated in table 2. The number of particles N is initiated for various test cases. The particles are initiated such that the distribution of the radii(r) of the particles follows a log-normal distribution $\left(\frac{e^{\left[\frac{M-\ln(r)}{2S^2}\right]}}{rS\sqrt{2\pi}}\right)$ with mean M and standard deviations S . The velocity ranges in x , y and z direction are denoted by V_x , V_y and V_z respectively. Parameters of distribution (M, S, N) and initiated velocity are varied for cases and stated in table 2. The particles initiated have random initial velocities with

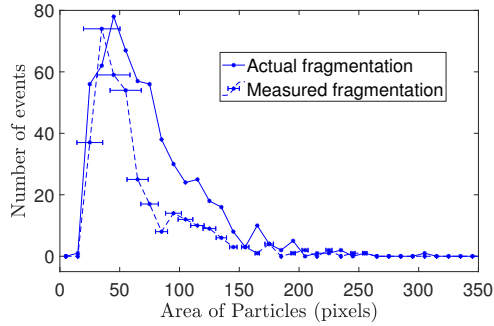
a Gaussian distribution. The procedure and constraints of image generation is detailed in appendix A.

Table 2 Parameter for images generated for validation

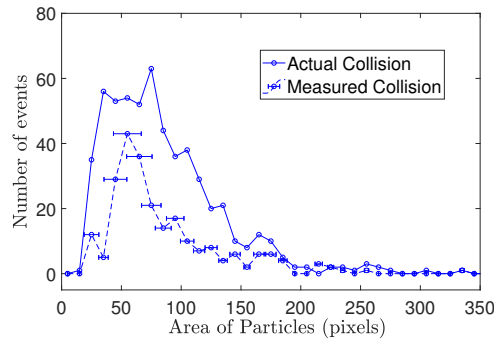
Test case.	Distribution parameters			Velocity		
	M	S	N	V_x	V_y	V_z
a	0.5	0.4	100	± 0.5	± 0.5	1 ± 0.5
b	0.3	0.4	100	± 0.5	± 0.5	1 ± 0.5
c	0.5	0.2	100	± 0.5	± 0.5	1 ± 0.5
d	0.5	0.4	200	± 0.5	± 0.5	1 ± 0.5
e	0.5	0.4	100	± 0.5	± 0.5	2 ± 1
f	0.5	0.4	100	± 1	± 1	1 ± 0.5

With synthetic images, all the results of fragmentation and collision events are known. These known results are compared with the results obtained from methodology stated in section 3.2 and 3.1. Even though the particles are kept spherical when not fragmenting and colliding, the change in area is observed along trajectories due to transverse velocity. The error in the area is small (around 5%) for a particle with an area greater than 20 pixels. Therefore collision/fragmentation of particles with a size greater than 20 pixels are compared. For particles larger than 20 pixels there is still variation in the area but of less than 5 %. The actual fragmentation/collision events of drops near the center of 3 dimensional domain (± 10 pixels) with Gaussian intensity variation around center (refer to appendix A for details) for all the cases stated in table 2 is compared with measured fragmentation/collision in figure 4.

The total number of measured fragmentation and collision events (on the vertical axis) for a particular area interval (on the horizontal axis) for all the cases is compared with actual fragmentation and collision events in figure 4(a) and figure 4(b) respectively. The area of the fragmented and collided particle is plotted in figure 4. **Based on the area, width and height of particle, the perimeter of the drop is calculated. Since the interface of the particle exists near the perimeter, error bar based on total number of pixels at the perimeter ($\approx \sqrt{4\pi A}$) is also plotted with measured events.** Comparing the actual and measured events reveals that not all the collisions and fragmentation are captured with the methodology described in the previous section. As stated in the previous section, the proposed method can capture the collision and fragmentation events of the particle with the approximate same size. After examining the results, it is found that when the resultant diameters ratio of new drops produced in fragmentation is in the range [0.27-0.78], the proposed method has an accuracy around 70%. For collision, if the ratio of minimum to the maximum diameter of the colliding drop is in the range [0.27-0.78], the proposed methods capture around 60% of collisions. Since we observed only two-dimensional images, only drops in the laser sheet while collision/fragmentation can be recorded and collision and collision/fragmentation events in



(a) Fragmentation events



(b) Collision events

Fig. 4 Comparison of actual fragmentation and collision events with measured fragmentation and collision events for drops with area ($A > 20$ pixels) and diameter ratio in range 0.27 to 0.78. The fragmentation and collision data for all the cases stated in table 2 is presented.

plane perpendicular to the laser sheet cannot be captured. With normal distribution used in image generation, the two dimensional method can capture upto 66% *i.e* two-thirds of the total events. Given the **constraints** with two-dimensional images, the efficiency (60%/66%) for collision is reasonably **good**. Approximately same collision and fragmentation efficiency was observed for all the cases stated in table 2. The limit of applicability ensures we capture only desired events and no false event.

4.2 Comparing velocity field from *Track* with optical flow method and volume fraction

For experiment D3V1, the comparison of results from Lagrangian methods with *Track* and for Eulerian methods for average volume fraction, average particle velocity (**normalized with the velocity at the nozzle**) in axial and radial direction is shown in figure 5. Since the attenuation effects after the breakup length (*i.e* after the potential core), do not significantly affect the drop detection, results after the breakup region is shown in figure 5. The average volume

fraction obtained from average image intensity (Eulerian approach) and with *Track* are shown in figure 5(a) and 5(b) respectively. The details of the procedure followed to calculate the average volume fraction is presented in appendix B. The intensity based volume fraction is obtained by averaging the intensity at each pixel. Similarity in volume fraction results between intensity based measurements and with *Track* can be observed in figure 5(a) and figure 5(b). The details of the procedure used for velocity from *Track* and optical flow are stated in appendix B and C respectively. In order to calculate the particle velocity from optical flow, the volume fraction from *Track* is required, one can refer to appendix C for details. From the comparison of the velocities in figures 5(c), 5(d), 5(e) and 5(f), we can conclude that the average particle velocity profile obtained from optical flow is approximately similar to the particle velocity from *Track*. This similarity in the axial and radial velocity confirms the validity of the average velocity and volume fraction obtained from *Track*. Similarly, results of the similar average velocity were obtained for all the cases stated in table 1, but are not presented here.

It can be observed from figure 5 that the average axial velocity and volume fraction is maximum at the center of the jet, and it decreases gradually to zero as the radial distance from the center-line increases. The average volume fraction and axial velocity also decays along flow and spreads as the axial distance from the nozzle increases. This decay is because of the entrainment of the surrounding fluid in the flow. Since fluid is entrained radially inwards, positive and negative value of the radial velocity are observed in figure 5.

4.3 Primary and Secondary Fragmentation results

The injector used in the experimental setup can only develop a jet for several seconds. The images are analyzed only after the time when the jet has reached its maximum unbroken length. This is done to exclude the transient part of the spray. After removal of the transient part, the analysis of 1500 images i.e around 1/6 of second is presented. In the present experiments, we have observed three regions of breakup, referred as A,B C and shown in figure 2(c). The first region A is the near nozzle region. A potential core of jet is present in region A and fragmentation has just initiated from the interface. After sufficient mass has been sheared from the interface in the first region, the remaining mass in the potential core breaks suddenly. This region B is the second region of fragmentation. Most of the fragmentation is observed in region A and B. After region B, drops flow in a self-similar velocity profile. This self-similar region of velocity is the region C. Observations of fragmentation and collision for different jets in this section are presented with reference to these regions.

The fragmentation from jet (assumed mostly due to injected fluid) is termed as primary fragmentation. The drop generated from primary fragmentation can further fragments in smaller drops due to its interaction with surrounding fluid, this phenomenon is therefore called secondary fragmentation. The visualization of primary and secondary fragmentation is also

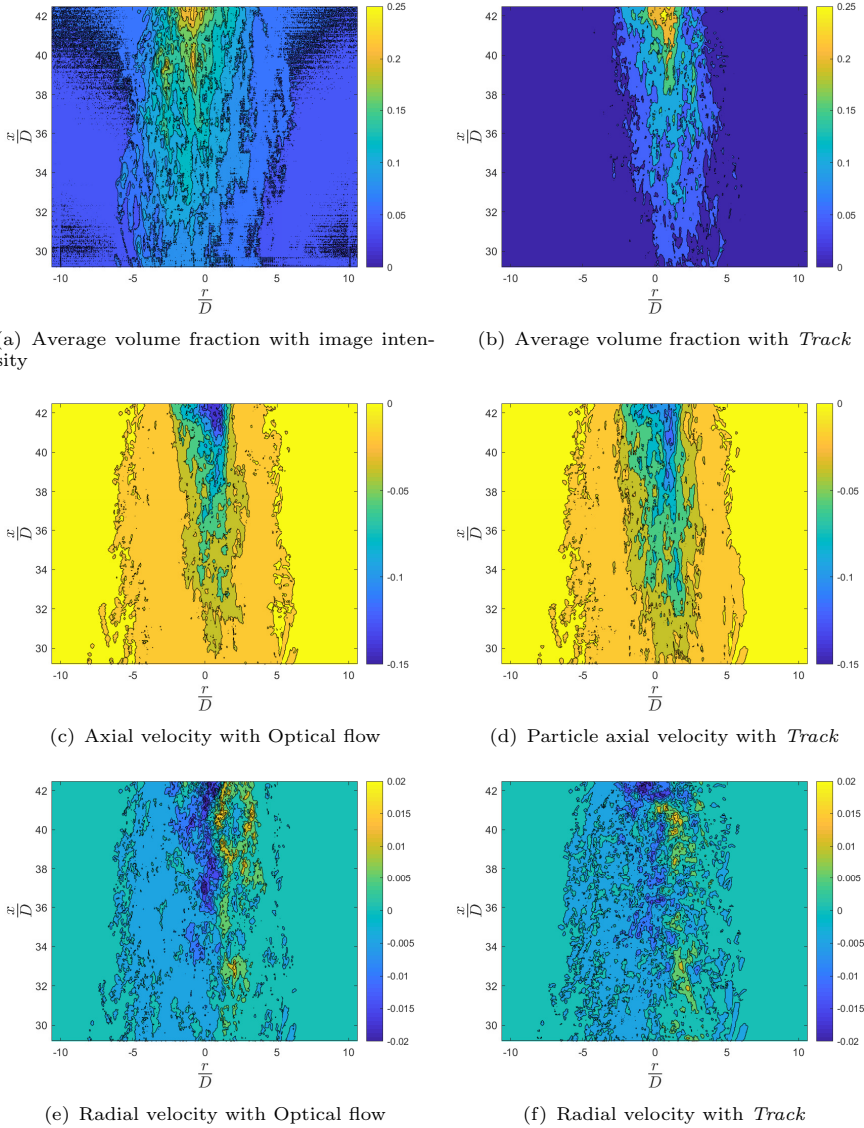


Fig. 5 Average Volume fraction \bar{Y} and Average Velocity comparison from Optical flow and *Track* for D3V1. The colorbar for velocity represents local velocity normalized with velocity at the nozzle outlet.

illustrated in figure 2(b). The process to identify secondary fragmentation is presented in section 3. Since the primary fragmentation is initiated near the interface of potential core (in region A), therefore the initial location of particle appearing in the first region can be considered as the location of primary fragmentation. However, after the region A *i.e* in region B, the particle appearance can be either due to fragmentation or transverse motion of the particle. The

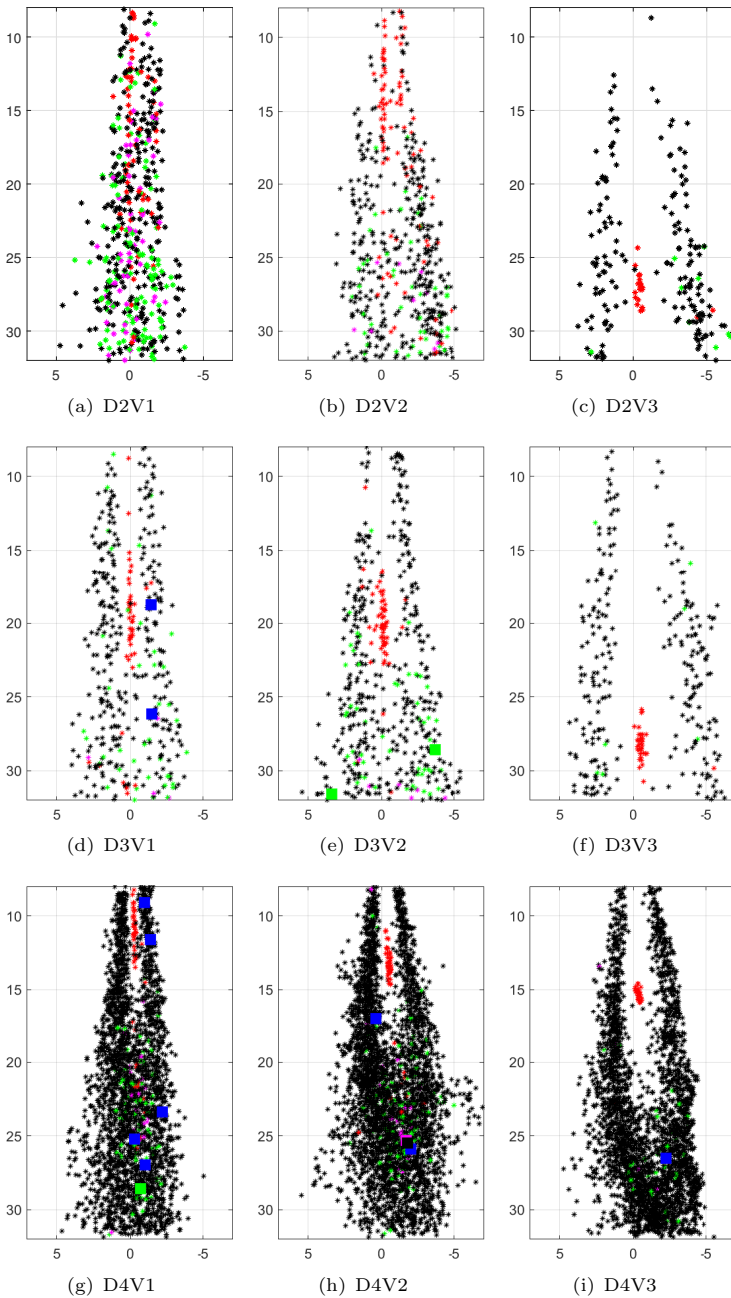


Fig. 6 Primary and Secondary fragmentation result for various experiments. Symbols: \star is used for primary fragmentation, \square is for secondary fragmentation. Size range for symbols is as follows: $20 \text{ pixels} < \leq D/10$; $D/10 < \star \leq D/2$; $D/2 < \star \leq 2D$; $2D < \star \leq 5D$; $\star > 5D$. The horizontal axis represents r/D and vertical axis represent x/D .

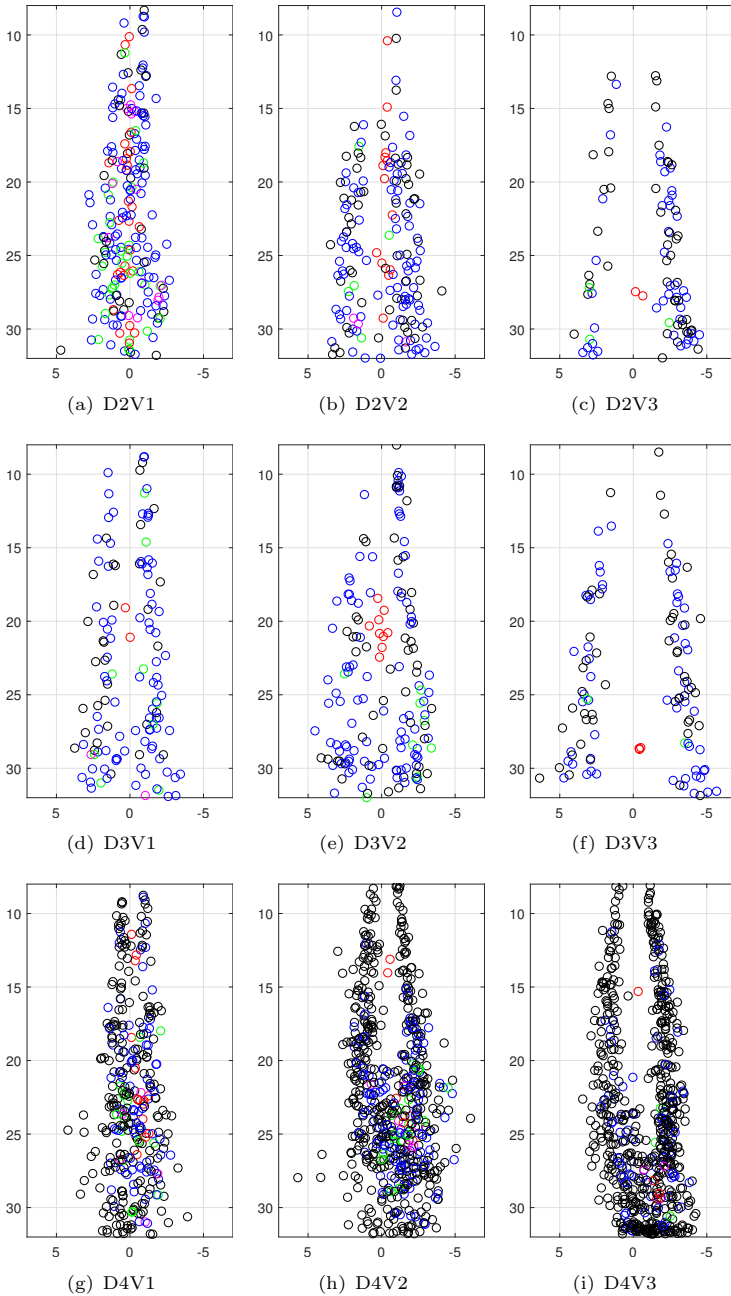


Fig. 7 Collision for various jets symbol: \circ . Size range for symbols is as follows: $20 \text{ pixels} < \circ \leq D/10$; $D/10 < \circ \leq D/2$; $D/2 < \circ \leq 2D$; $2D < \circ \leq 5D$; $\circ > 5D$. The horizontal axis represents r/D and vertical axis represent x/D .

size of each drop identified is calculated from the procedure stated in section 3.1. The location of primary and secondary fragmentation of the particle with different size particles for all the cases is shown in figure 6. The area of daughter particle after fragmentation for both primary and secondary fragmentation is represented by using different color symbols. The horizontal axis represents the normalized radial direction $\frac{r}{D}$ and vertical axis represents normalized axial direction $\frac{x}{D}$. Various symbols are used to denote the normalized size of the drop identified *i.e.* diameter of the drop normalized with the diameter of the nozzle of the jet.

The red star symbol(★), which represents drops of size $> 5D$ in figure 6 is representative of the potential core of the jet. The Reynolds number and Weber number of the jet increase (Re from 295 to 1813 and We from 179 to 5256) with an increase in velocity and diameter of the nozzle. With the increase in Reynolds number and Weber number, the breakup length of the jet increases. Therefore, the distance between the injector and the center of the potential core of the jet increases with an increase in velocity. The variation in the location of centroid of potential core denotes the oscillation/flapping of the unbroken part of the jet with time. The region in the figure 6 near the center of potential core indicates region A, as stated previously. In order to describe fragmentation zone *i.e.* region A and B, the axial region from $8D$ to $32D$ is plotted in figure 6.

Due to high uncertainty associated with drops of area less than 20 pixels, they are not shown in figure 6. It can be observed from all the figures that in the first region, black symbols that represents drop size greater than 20 pixels and smaller than $D/10$ are present. The number of smaller drops increases with Reynolds number. These smaller drop can either be due to small scale shear instability (Kelvin-Helmholtz type) or turbulence interaction of the surface or combination of both. Since with increase in velocity, the stable (non-fragmenting) size decreases to balance the inertia with surface tension of liquid, occurrence of higher number of smaller drop with increased Reynolds and Weber number is observed.

Primary atomization of large scale drops *i.e.* diameter range $[D/2 \leq D \leq 5D]$ are also observed for jets with lower Reynolds number. These larger drops are shown with green and magenta symbols in figure 6. The number of occurrence of drop with larger diameter decreases with increase in Reynolds number. The large scale drops are due to the large scale instability or bending of the jet and occur mostly in region B of the jet. In the second region, fragmented drops of various sizes are observed. Some results of secondary fragmentation can also be observed in the second region of the jet *i.e.* after the breakup length. It can also be observed from figure 6 that for high Reynolds number (with diameter D3 and D4), there are secondary fragmentation observed in the region of B of jet and whereas there is no secondary fragmentation for jet with diameter D2. In the present analysis, we were only able to identify some secondary fragmentation in the range of Reynolds and Weber numbers. But

the same procedure can be used to identify ternary fragmentation and thus analyze the cascade breakup.

4.4 Collision results

The results of daughter drop (resultant) sizes after collision are shown in figure 7. The symbols and vertical axis in figure 7 have same as used in figure 6. Due to oscillation and flapping of the potential core, the potential core disappears and reappears at approximately the same location. With the use of method 2 (based on birth and death events in section 3), the reappearance of the potential core of the jet with large shape deformity is identified as a collision. This spurious collision of the potential core is shown by red circles in fig. 7. In region A, the drop formed due to primary fragmentation, decelerate after detaching from the jet and since new drops are generated regularly from the interface. Therefore, collisions are also measured in region A despite a weak drop density. As only small drops are present in the first region of jet, small size collisions denoted by blue and black are observed here. In fact, the number of collision events is proportional to the square of droplet density [35]. In region B, a high density of drop exists of various sizes, therefore a large number of collision events of various sizes are measured. Later, as the drop approached towards region C, due to interaction of the drop with the surrounding fluid, more surrounding fluid is entrained in the jet. As the result of this entrainment, the jet spreads and drops decelerate. Due to the spreading of the jet, the density of the drop decreases, eventually causing decrease in number of collision. Since images view of the plot is selected such that only region A and B are shown fully in figure 7, this decrease in collision is slightly observed in jets with velocity V1.

4.5 Breakup analysis

Since the potential core of the jet is identified as a big drop, the breakup length of the jet (L_{break}) can be assessed. The variation of the breakup length normalized with the diameter of the jet (L_{break}/D_{jet}) is shown in figure 8. For single phase jets, the potential core can develop up to a distance $5D$ [36]. In the present case, the larger density ratio of 1.9 combined with surface tension effects extends the length of the potential core region to $10 - 50D$. Owing to the jet dynamics (bending instability) a variation in breakup length is observed and shown with error bars in fig. 8. A large variation of the breakup length is observed for low Reynolds jets, however as Reynolds number increases this variation decreases. With the increase in Reynolds number the breakup length increases. In particular, the breakup length of D2V3 seems to be very large as compared to other cases. At present, the reason for this behavior is unknown. Since there are various breakup mechanism acting simultaneously in the jet and dominance of the each usually characterized by the non-dimensional number [25] stated in equation 1. One of the possible reason for this non-linear variation of breakup length with velocity can be possibly due to intersection

or competition between various mechanism. This non-linear breakup length behaviour has been also previously reported by Lefebvre[37].

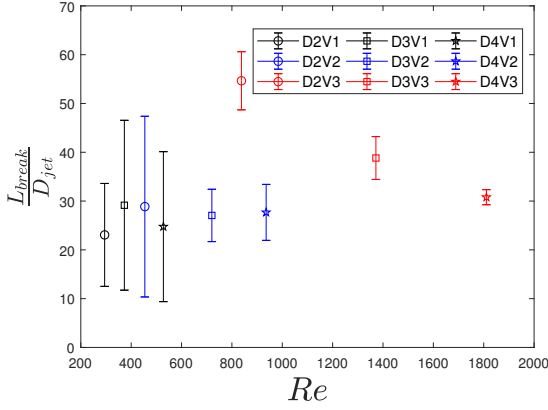


Fig. 8 Variation of Breakup length (normalized with the nozzle diameter) with Reynolds number for various jets stated in table 1

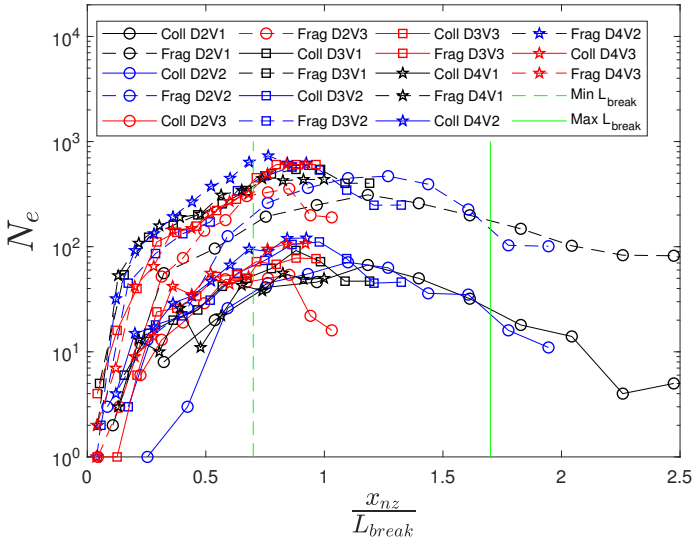


Fig. 9 Number of collision and fragmentation at various axial location. The symbols are representative of jet diameter and color are representative of inlet velocity of jet. Solid lines are used to shown the number of collision, whereas the dotted line is used to shown the number of primary fragmentation events.

Using the results of collision and primary fragmentation, the number of collision and fragmentation (N_e) with respect to the normalized distance to the nozzle (x_{nz}/L_{break}) is shown in figure 9. The axial position is discretized in 12 subregions of 100 pixels width. The number of events in each subregion is then summed. The maximum number of events for both collision and fragmentation occurs near the breakup length. Also, the number of fragmentation events are at least a order of magnitude larger than number of collision events.

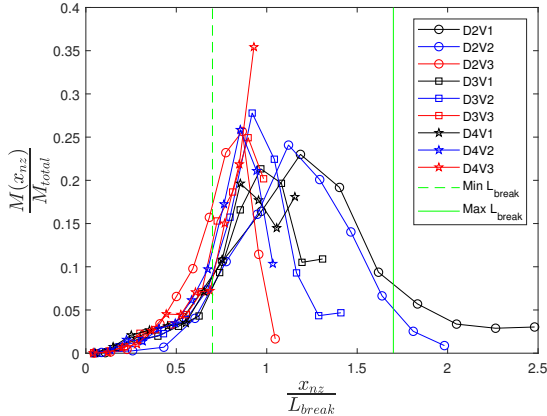


Fig. 10 Variation of fragmented mass fraction with axial location (normalized with breakup length) for jets stated in figure 1. Symbols represent diameter of the jet and color is the representation of the inlet velocity of the jet. The breakup region is shown with green lines.

The same discretization is applied on the fragmented mass distribution normalized with the total mass ($M(x_{nz})/M_{total}$) as shown in figure 10. In all experiments the fraction of fragmented mass initially increases with axial distance from the nozzle before reaching a maximum near the breakup region. More than 65% of the mass fragments in the breakup region.

5 Conclusion

In multiphase sprays, the dynamics of breakup and coalescence are difficult to investigate due to its opacity. To obtain two dimensional images of sprays at the center of multiphase phase, an experimental setup for studying spray (with density ratio 2) using an injected fluid with the same refractive index as the surrounding fluid is used in this paper. Mixing a fluorescent dye to injected fluid, the dynamics of the core of the spray becomes optically accessible, allowing recoding of images. A simple method to predict the characteristics of fragmentation, collision, velocity, and volume fraction from high-speed acquisition of images with software *Track* is developed. The developed method for collision and fragmentation is found to be accurate for particles with an area greater than 20 pixels and with a diameter ratio in the range 0.27 – 0.78. This sets the

limit of the pixel size to be used with the proposed methodology. The similarity between average Eulerian velocity from *Track* and optical flow in section 4.2 confirms the validity of results for volume fraction and velocity using *Track* in the far-field region of spray.

The results of primary/secondary fragmentation for various jets shows smaller drops are generated near the potential core and are possibly generated due to shear instability. Later the larger size drops are also generated as potential core breaks abruptly. With the present range of Reynolds number [295 – 1813] and Weber number [279 – 5256] and limited number of images, we are able to identify secondary fragmentation of the drops. No ternary fragmentation is found in the present experiments, but the stated methodology can be extended to found ternary breakup and later analyze the breakup cascade if it ever happens. Breakup length of two phase flow is found to be large as compared to single phase jet. Universal behavior of the variation of mass fraction fragmented, number of fragmentation events and number of collision events with axial distance is observed when normalized with breakup length.

Appendix A Image generation

A three-dimensional domain with dimensions 120 pixels (width) \times 200 pixels length in flow direction \times 40 units depth with N number of the particle initiated at random locations. The domain is set such that the particles going out the domain are entering again in the domain. The particle are reflected from the side walls (directions perpendicular to flow direction). The initial velocity of the particles at random locations is also initiated with the random velocity in any given interval. The initialized random velocity follows a uniform (Gaussian) distribution in the given interval. The velocity is positive in the flow direction. The initiated particles are allowed to flow with zero acceleration until there is collision or fragmentation. In order to model the fragmentation of particles, a fragmentation factor is assigned to each particle. This factor consists of a random constant (in interval 0 to 1) and is proportional to kinetic energy. As the flow progress, this factor increases and the particle is fragmented into two particles when the value of the fragmentation factor reaches a threshold value. The fragmentation threshold value of 5 is used for all cases. The radius and velocities of new particles are prescribed randomly while following the conservation of mass and momentum. For collision, distances between every two particles are calculated and compared with particle radius at each time to estimate their contact. Two particles are merged as soon as two particles are found in contact. The mass and momentum of the merging particle are also conserved. Since the synthetic images are used just to examine the procedure of collision and fragmentation, the shape of the particle is kept spherical at all the times, even while fragmentation and collision. To replicate the experimental condition, a Gaussian thickness of particle illumination along depth is included. For generating images, an averaged intensity along the depth is assigned to generate two dimensional images.

Appendix B Volume fraction and Eulerian particle velocity from *Track*

The Lagrangian information of particles can be used to obtain information about the volume fraction. Using the information about the location of centroid, width (W) and height (H) of an identified drop, the pixels occupied by the drop are assigned with the phase indicator function such that, $Y = 1$ if the drop is present in pixel else $Y = 0$. While plotting the phase indicator function we also use the approximation that its shape is approximated by an ellipse with it borders satisfying the equation $\frac{x_{pix}^2}{(0.5 \cdot W)^2} + \frac{y_{pix}^2}{(0.5 \cdot H)^2} = 1$. Using the indicator defined, the average volume fraction \bar{Y} over 1500 images for each pixel ($\bar{Y}(i, j) = \frac{1}{1500} \sum_{n=1}^{1500} Y(i, j; n)$). Using the Lagrangian velocity information, Eulerian information of velocity is also obtained. With *Track*, the particle velocity is directly obtained by substituting pixels with the velocity of particle occupied by it.

Appendix C Eulerian particle velocity from optical flow

The Farneback [38] optical flow methodology module in Matlab with an interrogative window size of 5 pixels is used. The velocity from optical flow (U_{of}) is obtained by solving equation C1 with the method stated by Farneback [38] optical flow as,

$$\frac{\partial g}{\partial t} + \nabla_{12} \cdot (g \langle U_{of} \rangle) = 0 \quad (\text{C1})$$

In equation C1, g is the intensity measured by detector and ∇_{12} and is the spatial gradient in two directions. Liu and Shen[39] in their detailed derivation for optical flow with laser sheet-induced fluorescence have stated the expression for U_{of} as, $U_{of} = \frac{\int \phi U_{12} dV}{\int \phi dV}$ where ϕ is the scalar concentration in flow (e.g. dye), or particle number per unit total volume for particulate flows. Since fluorescence is recorded only at the pixels occupied by the particle, therefore $\int \phi U_{12} dV = U_p$ and $\int \phi dV = \bar{Y}$, here U_p is the average velocity of particle and \bar{Y} is the volume fraction in the interrogation window. \bar{Y} can be calculated with the procedure stated in appendix B. Using the simplifications stated, the particle velocity from Optical flow can be stated as $U_p = U_{of} \cdot \bar{Y}$.

Acknowledgments

The Experiments were performed under the research program on nuclear safety and radioprotection (RSNR). The experiments were funded from French government managed by the National Research Agency (ANR) under Future Investments Program (PIA), research grant No: ANR-10-RSNR-01. The authors are grateful to Engineering Department of LEMTA for their support

on the development of the experimental setup. The purchase of *Track* was funded by the research grant PALAGRAM granted by the French National Research Agency (ANR-19-CE30-0041). The authors also acknowledge partial support from COST action MP1305 "Flowing Matter", supported by COST (European Cooperation in Science and Technology).

The authors report no conflict of interest.

References

- [1] Elhimer, M., Praud, O., Marchal, M., Cazin, S., Bazile, R.: Simultaneous piv/ptv velocimetry technique in a turbulent particle-laden flow. *Journal of Visualization* **20**(2), 289–304 (2017)
- [2] Blaisot, J., Yon, J.: Droplet size and morphology characterization for dense sprays by image processing: application to the diesel spray. *Experiments in fluids* **39**(6), 977–994 (2005)
- [3] Malot, H., Blaisot, J.-B.: Droplet size distribution and sphericity measurements of low-density sprays through image analysis. *Particle & Particle Systems Characterization: Measurement and Description of Particle Properties and Behavior in Powders and Other Disperse Systems* **17**(4), 146–158 (2000)
- [4] Nishino, K., Kato, H., Torii, K.: Stereo imaging for simultaneous measurement of size and velocity of particles in dispersed two-phase flow. *Measurement Science and Technology* **11**(6), 633 (2000)
- [5] Asgarian, A., Yang, Z., Tang, Z., Bussmann, M., Chattopadhyay, K.: An image feature consolidation technique (ifct) to capture multi-range droplet size distributions in atomizing liquid sheets. *Experiments in Fluids* **61**(1), 1–22 (2020)
- [6] Kashdan, J.T., Shrimpton, J.S., Whybrew, A.: A digital image analysis technique for quantitative characterisation of high-speed sprays. *Optics and Lasers in Engineering* **45**(1), 106–115 (2007)
- [7] Akhmetbekov, Y.K., Alekseenko, S.V., Dulin, V.M., Markovich, D.M., Pervunin, K.S.: Planar fluorescence for round bubble imaging and its application for the study of an axisymmetric two-phase jet. *Experiments in Fluids* **48**(4), 615–629 (2010)
- [8] Crimaldi, J.: Planar laser induced fluorescence in aqueous flows. *Experiments in fluids* **44**(6), 851–863 (2008)
- [9] Dunand, P., Castanet, G., Gradeck, M., Maillet, D., Lemoine, F.: Energy balance of droplets impinging onto a wall heated above the leidenfrost temperature. *International Journal of Heat and Fluid Flow* **44**, 170–180

(2013)

- [10] Deshmukh, D., Ravikrishna, R.: A method for measurement of planar liquid volume fraction in dense sprays. *Experimental thermal and fluid science* **46**, 254–258 (2013)
- [11] Desantes, J., Pastor, J., Pastor, J., Julia, J.: Limitations on the use of the planar laser induced exciplex fluorescence technique in diesel sprays. *Fuel* **84**(18), 2301–2315 (2005)
- [12] Kannaiyan, K., Banda, M.V.K., Vaidyanathan, A.: Planar sauter mean diameter measurements in liquid centered swirl coaxial injector using laser induced fluorescence, mie scattering and laser diffraction techniques. *Acta Astronautica* **123**, 257–270 (2016)
- [13] Koegl, M., Mishra, Y.N., Baderschneider, K., Conrad, C., Lehnert, B., Will, S., Zigan, L.: Planar droplet sizing for studying the influence of ethanol admixture on the spray structure of gasoline sprays. *Experiments in Fluids* **61**(10), 1–20 (2020)
- [14] Zimmer, L., Domann, R., Hardalupas, Y., Ikeda, Y.: Simultaneous laser-induced fluorescence and mie scattering for droplet cluster measurements. *AIAA journal* **41**(11), 2170–2178 (2003)
- [15] Kristensson, E., Berrocal, E., Richter, M., Pettersson, S.-G., Aldén, M.: High-speed structured planar laser illumination for contrast improvement of two-phase flow images. *Optics letters* **33**(23), 2752–2754 (2008)
- [16] Abu-Gharbieh, R., Persson, J.L., Försth, M., Rosen, A., Karlström, A., Gustavsson, T.: Compensation method for attenuated planar laser images of optically dense sprays. *Applied Optics* **39**(8), 1260–1267 (2000)
- [17] Chigier, N.: Drop size and velocity instrumentation. *Progress in Energy and Combustion Science* **9**(1-2), 155–177 (1983)
- [18] Cierpka, C., Lütke, B., Kähler, C.J.: Higher order multi-frame particle tracking velocimetry. *Experiments in Fluids* **54**(5), 1–12 (2013)
- [19] Wu, P.-H., Agarwal, A., Hess, H., Khargonekar, P.P., Tseng, Y.: Analysis of video-based microscopic particle trajectories using kalman filtering. *Biophysical journal* **98**(12), 2822–2830 (2010)
- [20] Kearney, R.V., Bewley, G.P.: Lagrangian tracking of colliding droplets. *Experiments in Fluids* **61**(7), 1–11 (2020)
- [21] Bordás, R., Roloff, C., Thévenin, D., Shaw, R.: Experimental determination of droplet collision rates in turbulence. *New Journal of Physics* **15**(4),

045010 (2013)

- [22] Désécures, M., Baude, R.: APREX Solutions. <https://www.aprex-solutions.com/fr/>
- [23] Déchelette, A., Babinsky, E., Sojka, P.: Drop size distributions. In: Handbook of Atomization and Sprays, pp. 479–495. Springer, ??? (2011)
- [24] Gorokhovski, M., Herrmann, M.: Modeling primary atomization. *Annu. Rev. Fluid Mech.* **40**, 343–366 (2008)
- [25] Villermaux, E.: Fragmentation. *Annu. Rev. Fluid Mech.* **39**, 419–446 (2007)
- [26] Hadj-Achour, M., Rimbart, N., Gradeck, M., Meignen, R.: Fragmentation of a liquid metal droplet falling in a water pool. *Physics of Fluids* **33**(10), 103315 (2021)
- [27] Brochard, F., Shalpegin, A., Bardin, S., Lunt, T., Rohde, V., Briançon, J., Pautasso, G., Vorpahl, C., Neu, R., *et al.*: Video analysis of dust events in full-tungsten asdex upgrade. *Nuclear Fusion* **57**(3), 036002 (2016)
- [28] Brochard, F., Rohde, V., Lunt, T., López, G.S., Shalpegin, A., Neu, R., Team, A.U.: Intrinsic dust transport in asdex upgrade studied by fast imaging. *Nuclear Materials and Energy* **18**, 268–274 (2019)
- [29] Von der Linden, W., Dose, V., Von Toussaint, U.: Bayesian Probability Theory: Applications in the Physical Sciences. Cambridge University Press, ??? (2014)
- [30] Yagoh, K., Ogawara, K., Iida, S.-i.: The particle tracking method using the kalman filter. In: Flow Visualization VI, pp. 838–842. Springer, Berlin, Heidelberg (1992)
- [31] Metivier, C., Brochard, F., Darbouli, M., Magnin, A.: Oscillatory rayleigh-bénard convection in elasto-viscoplastic gels. *Journal of Non-Newtonian Fluid Mechanics* **286**, 104428 (2020)
- [32] Ou, W., Brochard, F., Morgan, T.: Bubble formation in liquid sn under different plasma loading conditions leading to droplet ejection. *Nuclear Fusion* **61**(6), 066030 (2021)
- [33] Hsiang, L.-P., Faeth, G.M.: Near-limit drop deformation and secondary breakup. *International journal of multiphase flow* **18**(5), 635–652 (1992)
- [34] Rimbart, N., Escobar, S.C., Meignen, R., Hadj-Achour, M., Gradeck, M.: Spheroidal droplet deformation, oscillation and breakup in uniform outer flow. *Journal of Fluid Mechanics* **904** (2020)

- [35] Elimelech, M., Gregory, J., Jia, X.: Particle Deposition and Aggregation: Measurement, Modelling and Simulation. Butterworth-Heinemann, ??? (2013)
- [36] Or, C., Lam, K.M., Liu, P.: Potential core lengths of round jets in stagnant and moving environments. *Journal of Hydro-environment Research* **5**(2), 81–91 (2011)
- [37] Lefebvre, A.H., McDonell, V.G.: Atomization and Sprays. CRC press, ??? (2017)
- [38] Farnebäck, G.: Two-frame motion estimation based on polynomial expansion. In: *Scandinavian Conference on Image Analysis*, pp. 363–370 (2003). Springer
- [39] Liu, T., Shen, L.: Fluid flow and optical flow. *Journal of Fluid Mechanics* **614**, 253–291 (2008)